Engineering Fracture Mechanics 344 (2026) 112383

Contents lists available at ScienceDirect

Engineering Fracture Mechanics

journal homepage: www.elsevier.com/locate/engfracmech

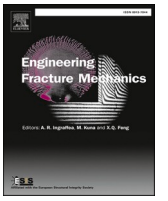

Defect-based fatigue life prediction of A356-T6 aluminium alloy wheels

Nicola Zani [a], Candida Petrogalli [a], Silvio Bonometti [a], Nicola Ferrami [b], Alessandro Concoreggi [b], Alessio Franchi [b], Claudio Sorlini [b], Giorgio Donzella [a,*]

[a] Department of Mechanical and Industrial Engineering, University of Brescia, Via Branze, 38, 25123 Brescia, Italy
[b] Cromodora Wheels S.p.A., Via Montichiari 20, 25016 Ghedi, BS, Italy

ARTICLE INFO

Keywords:
Fatigue life
Fatigue limit
Small cracks
Extreme value statistics
A356 alloy wheel

ABSTRACT

This study presents a defect-tolerant methodology for the fatigue assessment of full-scale A356-T6 cast aluminium wheels, explicitly accounting for the influence of casting defects on crack initiation and early propagation. The approach combines rotating-bending fatigue tests on complete wheels, finite-element identification of the fatigue-critical spoke region, metallographic characterization of shrinkage porosity, extreme-value statistical analysis of the maximum Feret diameter, and local residual-stress measurements by hole drilling. The statistically expected maximum defect size in the critical region was subsequently used as the initial defect in a small-crack-based predictive framework, in which the effect of mean stress was included through the measured residual-stress field. To address the requirements of industrial fatigue design, the defect statistics were extended from the single spoke to increasing return periods corresponding to one wheel and to production batches, allowing the derivation of lower-bound S-N predictions representative of increasing production volumes. The results show that the proposed framework captures the experimentally observed fatigue behaviour and provides conservative fatigue thresholds consistent with the statistical occurrence of critical defects. The methodology therefore offers a physically grounded and industrially applicable tool for defect-tolerant design and quality control of safety–critical cast components.

1. Introduction

Cast Al-Si-Mg aluminium alloys, particularly A356-T6, are extensively used in the automotive industry due to their favourable strength-to-weight ratio, excellent castability and corrosion resistance. These alloys are widely adopted for structural components such as wheels, where reducing unsprung mass is critical for improving handling, braking efficiency and fuel economy. However, their fatigue performance remains a major design constraint due to the intrinsic presence of casting defects such as shrinkage porosity and non-metallic inclusions, which act as potential crack initiation sites under cyclic loading. Extensive research by several authors [1–6] has demonstrated that the fatigue crack initiation in these alloys is a complex phenomenon governed by the critical competition between microstructural features and the dominant casting defects. Consequently, the fatigue behaviour of cast components is strongly governed by the size and morphology of these internal defects, rather than the nominal strength of the matrix material.

Considering internal defects as inherent small cracks, a first contribution by Murakami [7] introduced the use of the $\sqrt{area}$

* Corresponding author.
E-mail address: giorgio.donzella@unibs.it (G. Donzella).

https://doi.org/10.1016/j.engfracmech.2026.112383
Received 5 March 2026; Received in revised form 8 June 2026; Accepted 17 June 2026
Available online 18 June 2026

parameter as a substitute for equivalent crack size, establishing a direct relationship between the fatigue limit and the projected area of inclusions or voids. His model enables a unified treatment of surface and subsurface defects using a fracture mechanics framework and has since become a widely adopted method in fatigue design. More recently, Murakami and Endo [8,9] have broadened this approach by introducing a practical small-crack model that can reproduce an entire fatigue life curve even when only very limited fatigue data exist. Their idea is that the fatigue limit gradually drops as the defect or crack grows, and this simple mechanical mechanism is enough to capture the overall shape of the curve.

In defect-based fatigue assessment, the characteristic size of a flaw can be quantified by either the $\sqrt{area}$ parameter, as adopted in Murakami's framework [7], or by the maximum Feret diameter. The $\sqrt{area}$ parameter reflects the projected area of the defect on a plane perpendicular to the principal stress and it is suitable for inclusion-like discontinuities; on the other hand, the Feret diameter measures the maximum linear extent of a flaw and is therefore more sensitive to elongated or branched geometries. This distinction is significant for A356 castings, where shrinkage porosities frequently exhibit highly irregular interdendritic shapes. The severe notch effect and stress concentration induced by the 3D morphology of these shrinkage pores have been thoroughly investigated through advanced characterization techniques such as X-ray tomography and microstructural modelling [10–12]. This geometric complexity is directly linked to the manufacturing technology; indeed, for components produced via Low Pressure Die Casting (LPDC), recent investigations [13] have highlighted how specific defect populations, primarily shrinkage porosities and oxide films, dictate the overall fatigue properties. As noted by Tebaldini et al. [14], the Feret diameter of shrinkage pores is often substantially larger than the corresponding $\sqrt{area}$ parameter and correlates more consistently with the observed fatigue behaviour.

Recent developments in probabilistic defect modelling have leveraged extreme value statistics to quantify the likelihood of encountering the most detrimental defects within a given component volume. Pioneering works on stochastic fatigue modelling [15] have demonstrated the necessity of linking the defect size distribution directly to the failure probability of cast components. Furthermore, Beretta [16] provides a comprehensive review of more than two decades of applying this methodology to fatigue-critical components, including cast and additively manufactured metals.

Despite the availability of these analytical tools, most fatigue studies on A356-T6 alloys rely on small-scale specimens machined from castings, often overlooking the geometric stress amplifications, residual stress fields and surface conditions inherent in full-scale components. In this respect, Tebaldini et al. [14] provided an important advancement by testing complete wheels in their final state under rotating bending loads, thus capturing realistic conditions. They investigated the fatigue response of full-scale A356-T6 wheels through a combined use of bending tests, finite-element stress analysis, and metallographic defect characterization. Using Gumbel extreme-value statistics, the authors estimated the maximum shrinkage-porosity size likely to occur within the fatigue-critical regions of the spokes. The predicted defect sizes were then correlated with crack-initiation lives obtained both from natural casting defects and from artificial holes introduced to reproduce critical pore dimensions. Furthermore, recent studies on Al-Si-Mg cast alloys under rotating bending have detailed the specific crack initiation and short-crack propagation behaviours [17], reaffirming that subsurface and surface defects act as the primary drivers for fatigue failure under macroscopic bending moments. Wang et al. [18] proposed an integrated finite-element-based framework to predict the fatigue life of A356 aluminium wheels by coupling casting-process simulations with structural analysis. Their approach explicitly accounts for porosity and secondary dendrite arm spacing (SDAS) through mesh-mapping techniques. In parallel, multi-scale modelling approaches have been recently developed to link microstructural features and casting defects to macroscopic fatigue performance [19], further highlighting the need to link the gap between material properties and full-scale component behaviour. While these methodologies represent a significant advancement toward through-process fatigue modelling, they remain largely numerical and do not incorporate experimentally measured defect statistics, residual stress fields, or defect-based fracture-mechanics formulations.

From an industrial perspective, the relevance of realistic loading conditions in wheel fatigue assessment has been recently emphasized by Allouch et al. [20], who reviewed the influence of test methods, load spectra, and wheel–tire configurations on fatigue results. Their work highlights that conventional radial and cornering fatigue tests may not fully reproduce service-like multiaxial loading conditions, and that test constraints can significantly affect local stress states and fatigue outcomes. Zanchini et al. [21] investigated fatigue and failure mechanisms in both aluminium and composite wheels. Similar life prediction challenges and failure analyses have also been addressed in forged 6061 aluminium wheels [22] and in the in-service fatigue evaluation of heavy-duty wheels [23], highlighting how different manufacturing techniques (casting and forging) require adapted approaches to account for their distinct microstructural features and inherent defect populations. These results emphasize the interplay between material system, geometry, and manufacturing route, showing that even components with non-negligible defect populations can pass homologation standards if local stress fields and defect locations are appropriately managed.

More recently, three complementary reviews have provided a consolidated framework for interpreting defect-controlled fatigue in cast and wrought metals. The first two parts of the investigation by Zerbst et al. [24,25] present a systematic description of the different stages of short-crack growth, the conditions for crack arrest, and the dependence of the critical defect size on material strength and local microstructure. These works also clarify when a defect should be treated as a crack and when its notch-like character must be retained, an aspect of practical importance for cast aluminium components. This is further supported by specific investigations on the fatigue crack growth thresholds and microstructural barriers in cast aluminium [26], which highlight the role of the eutectic network in resisting crack propagation. Additionally, Serrano-Muñoz et al. [27] offers an experimental perspective by directly comparing the fatigue behaviour of surface and internal defects in A357-T6 alloy under controlled air and vacuum conditions. Their results show that large internal defects do not necessarily reduce fatigue life when the crack propagates in an airtight environment, whereas surface-breaking defects lead to markedly shorter lives due to environmentally assisted crack growth. Collectively, these studies reinforce the view that the fatigue performance of cast Al–Si–Mg alloys is governed not only by defect size but also by defect location, local stress

state and the mechanisms controlling short-crack propagation.

The present study addresses this gap by proposing an experimentally validated defect-tolerant methodology for the fatigue assessment of full-scale A356-T6 automotive wheels. The methodology integrates rotating-bending tests on complete wheels, finite-element identification of the fatigue-critical region, local residual-stress measurements and extreme-value statistics of casting defects within a unified small-crack-based framework. In this way, the statistically expected defect size is linked to the local stress condition and to the fatigue behaviour of the actual component, rather than of a simplified specimen. The methodology is specifically aimed at deriving lower-bound fatigue predictions for progressively larger return periods and production volumes, thus offering a practical basis for the design and quality control of safety–critical cast components.

2. Wheel material and manufacturing

The wheels analysed in this study were manufactured from A356-T6 aluminium alloy and supplied by Cromodora Wheels S.p.A. The geometry of the tested components corresponded to the configuration shown in Fig. 1. The tested component is a 10-spoke wheel, 20 in. in diameter, with a 9-inch rim channel width. Each spoke has an overall height of approximately 38 mm, while its width varies from about 30 mm in the upper region to about 15 mm in the lower section. The alloy's nominal chemical composition, expressed in weight percent, is reported in Table 1, while Table 2 lists the mechanical properties obtained from tensile tests performed on specimens extracted from the spoke area. Tebaldini et al. [14] reported a fatigue-limit value of 117.5 ± 14.12 MPa at 500,000 cycles for A356-T6 wheels manufactured by the same production process and tested under rotating bending. Vickers hardness was also measured, as this parameter is required by the defect-based predictive models employed in the present work. To ensure consistent material behaviour and stable processing conditions, a dedicated production batch of the wheel variant under investigation was prepared.

All wheels were produced in a single controlled manufacturing cycle to guarantee uniform properties for the fatigue experiments. Casting was performed through Low Pressure Die Casting (LPDC), a technique that limits turbulence in the molten aluminium and promotes directional solidification, thereby reducing the formation of gas porosity and shrinkage defects. After solidification, the components underwent the standard T6 heat treatment [14]. This treatment favours Mg_2Si precipitation, improving the alloy's strength and enhancing its fatigue resistance. Subsequent machining operations, such as turning and drilling, were carried out to achieve the required dimensional accuracy. Particular attention was paid to preserving the compressive residual stresses generated during quenching, especially in areas sensitive to fatigue.

A portion of the wheels from the same production batch was set aside for metallographic analysis aimed at characterising the defect distribution in fatigue-critical regions identified through finite-element simulations. The resulting defect statistics were used as input for extreme-value analysis and provided the initial flaw sizes for the fracture-mechanics models described later. The remaining wheels were subjected to bending fatigue tests to investigate crack initiation mechanisms and endurance behaviour under service-representative cyclic loading.

3. Experimental fatigue tests and numerical model of the wheel

Fatigue life, including both the fatigue limit and the finite-life region, was experimentally assessed using the MAKRA test bench (shown in Fig. 2), in accordance with the SAE J328 standard [28]. Tests were conducted under load-controlled conditions with a fully reversed loading ratio ($R = -1$) up to one million cycles.

A test was considered to have failed when a fatigue crack of 2 mm in length appeared within the most critical region of the wheel. This criterion is consistent with standard industrial practices for bending fatigue assessment and ensures comparability with homologation requirements. To better identify the crack appearance during testing, the wheels were coated with a mixture of zinc oxide and glycerol before being mounted on the machine.

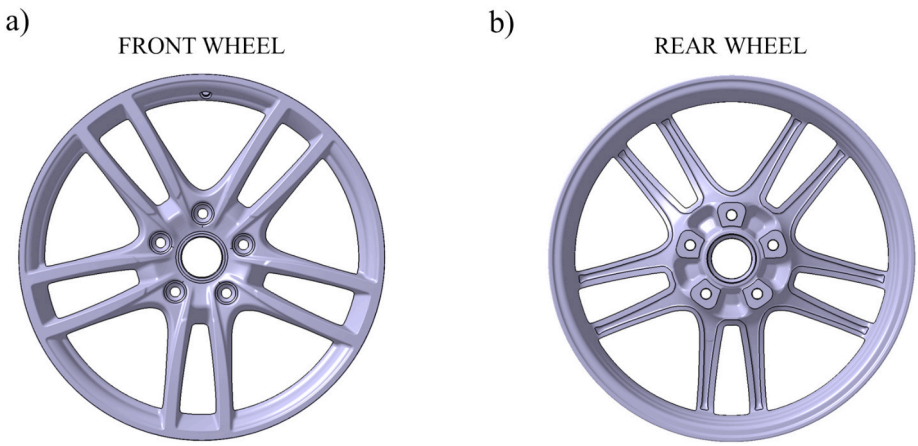

Fig. 1. Wheel geometry used for the experimental and numerical analyses: a) front wheel; b) rear wheel.

Table 1
Chemical composition (wt.%) of the A356 aluminium alloy used in this study [14].

Alloy	Si	Mg	Sr	Ti	Fe	Cu, Zn, Mn	Al
A356	6.840	0.273	0.015	0.118	0.088	<0.01	Bal.

Table 2
Mechanical properties and microstructural parameters of the A356-T6 alloy [14].

UTS [MPa]	YS [MPa]	Elongation [%]	Vickers hardness [HV]
257 ± 5	207 ± 5	4.0 ± 0.7	94

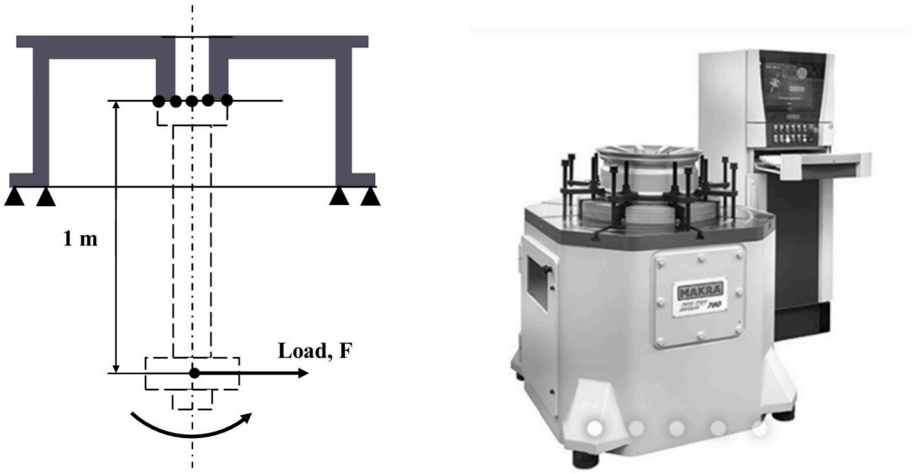

Fig. 2. MAKRA rotating bending test bench used for the experimental fatigue campaign.

A finite element model was developed in Abaqus® to simulate the rotating bending fatigue test applied to the wheel. The wheel geometry was discretised using 3D quadratic tetrahedral solid elements, resulting in approximately 1 million elements. The simulation replicates the actual boundary conditions of the experimental setup: the rim is fully constrained, and a cyclic bending moment of constant amplitude is applied at the central hub through a node rigidly connected to the coupling flange. The load reproduces one full revolution of the applied moment, thereby capturing the stress variation experienced by the wheel during real operating conditions. The material behaviour was assumed to be linear elastic, with Young's modulus and Poisson coefficients equal to 70 GPa and 0.3, respectively. The mesh was refined in the areas of interest to ensure accurate stress evaluation.

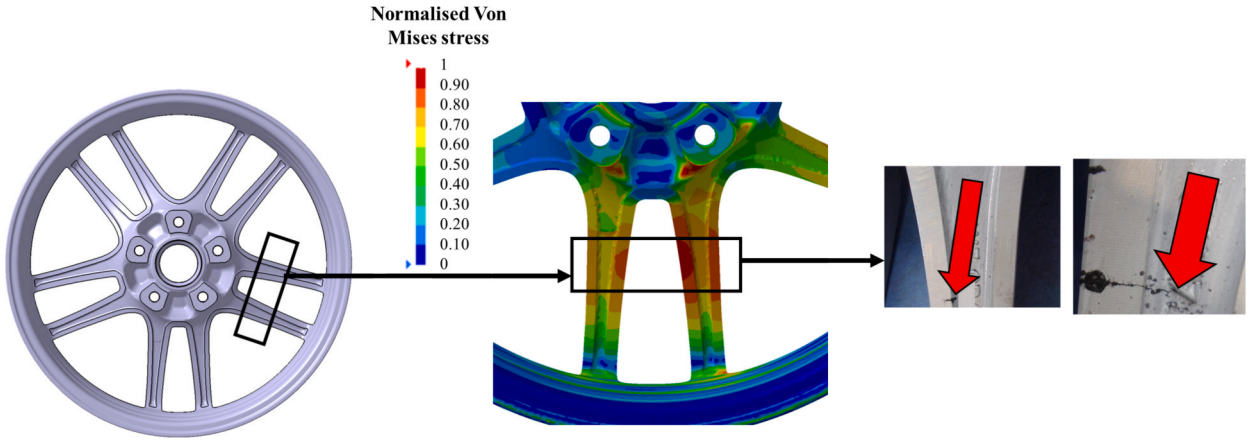

Fig. 3. Identification of the fatigue-critical spoke region: overall wheel geometry with indication of the investigated area (left), FEA distribution of Von Mises stress normalised with respect to the maximum value, highlighting the same critical spoke region (centre) and experimental evidence of crack initiation in the corresponding region during bending fatigue tests (right).

Both experimental tests and the numerical analysis highlighted the most critical zone in a region located approximately at the midsection of the spoke, on the side facing the hub: in fact, wheel failures happened in this zone, which also exhibits the highest stresses predicted by the finite element model (Fig. 3). The concentration of stress in this region is influenced by the local geometry and load path distribution during bending. In the selected critical spoke region, the local stress cycle is almost fully reversed. Moreover, the maximum principal stresses act in the radial direction (aligned with the spoke axis) and are orthogonal to the observed fracture plane.

This convergence between experimental and simulated failure locations validates the model and justifies the selection of this region for subsequent metallographic inspection and defect-based fatigue analyses.

The fatigue test results are summarized in Fig. 4. In this figure, each stress level is defined in terms of the maximum radial stress estimated in the most critical zone of the spoke through the finite element model, when the corresponding experimental bending moment is applied to the wheel. For confidentiality reasons related to industrial secrecy, the radial values shown on the vertical axis of the figure are normalised with respect to the minimum experimental stress level, rather than reported in absolute terms.

In the plot, open markers indicate those stress levels at which the specimens reached the estimated run-out without exhibiting any detectable fatigue damage, whereas solid markers denote stress levels for which the wheels failed before achieving the run-out threshold.

Fig. 5 presents a SEM micrograph of the spoke fracture surface, together with a close-up of the crack-initiation region. The morphology is consistent with fatigue-induced failure. In all examined specimens, crack initiation originated from a localized sub-surface porosity, which acted as a stress intensifier and promoted crack nucleation under cyclic loading.

4. Statistical characterization of casting defects (Extreme value Analysis)

Specimens for the defect analysis were extracted from the spoke cross-section corresponding to the actual fracture zone, which coincides with the one predicted by the FEA. Specimen preparation followed standard metallographic procedures (ASTM E3-11 [29]) and optical microscopy combined with Axiovision (Zeiss) image analysis software was used to quantify defect geometry, including the maximum Feret diameter. For each specimen, 100 micrographs were collected in random orientations, covering a total inspected area of 120 mm^2. The magnification was selected to capture entire defect clusters and to distinguish among different types of casting flaws such as gas porosity, shrinkage cavities, and oxide films. The microstructure displayed the typical dendritic morphology of A356 castings, with a primary α-aluminium matrix surrounded by a eutectic Al-Si network. Shrinkage pores were recognised as primary inherent defects (see Fig. 6).

A statistical analysis of the shrinkage pores population was carried out following ASTM E2283-03 standard [30] and ESIS P11-02 recommendations [31]. The experimental distributions of the largest observed pores were well described by the Gumbel extreme value distribution [32], expressed as:

$$F(x) = \exp\left(-\exp\left(-\frac{x-\lambda}{\delta} \right) \right) \tag{1}$$

where x is the maximum Feret diameter, λ is the location parameter, and δ is the scale parameter. To construct the Gumbel plot, the maximum Feret diameters measured in the sampled inspection fields were ranked in ascending order, $x_1 \le x_2 \le \cdots \le x_n$. An empirical cumulative probability was then assigned to each ranked value according to:

$$F_j = \frac{j}{n+1} \tag{2}$$

where $j = 1, 2, \cdots, n$ and n is the total number of sampled fields. The corresponding Gumbel reduced variates were calculated as:

$$y_i = -\ln\left[-\ln(F_j) \right] \tag{3}$$

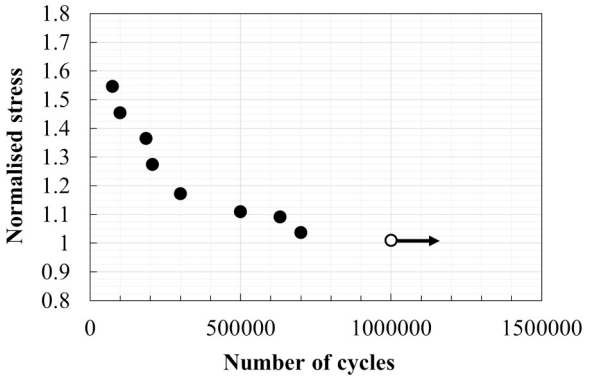

Fig. 4. Normalised stress versus number of cycles for the rotating bending fatigue tests. Solid markers indicate failures; open markers represent run-outs.

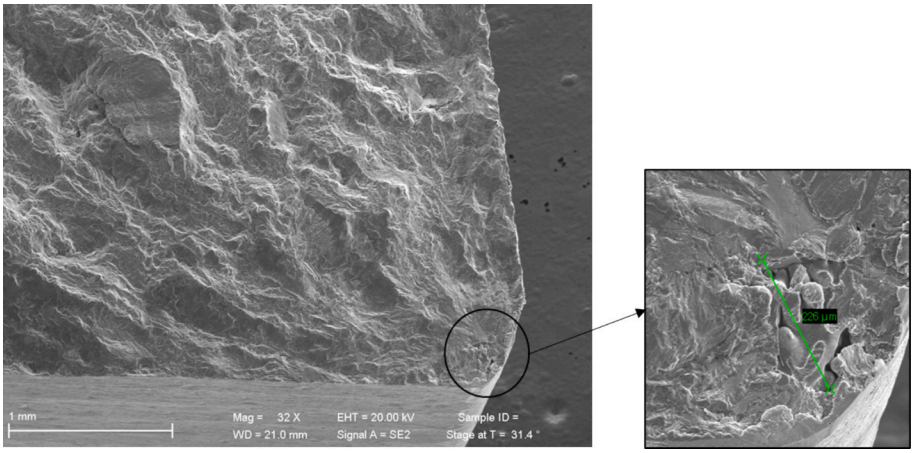

Fig. 5. SEM observations of spoke's fracture surfaces (normalised stress 1.06, number of cycles to failure about 950000).

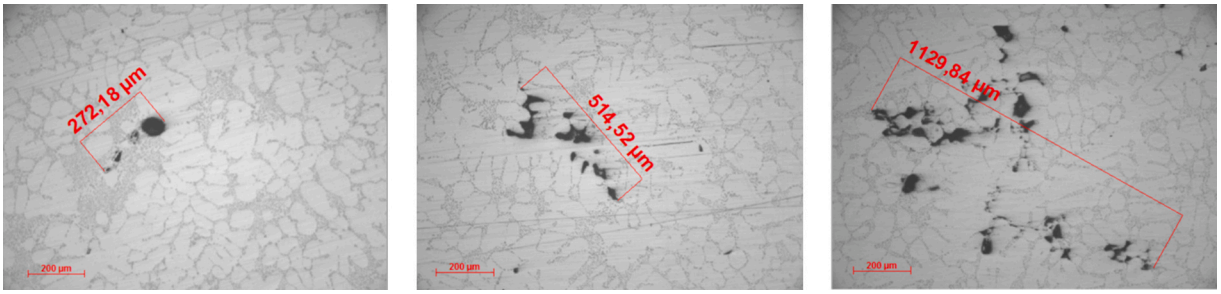

Fig. 6. Metallographic images of the A356-T6 microstructure showing examples of shrinkage pore cluster.

In Gumbel coordinates, the experimental data are expected to follow a linear relationship of the form:

$$x_j = \lambda + \delta y_j \tag{4}$$

The parameters λ and δ were estimated using the Moments method:

$$\delta = \frac{\pi}{\sqrt{6}} s \tag{5}$$

$$\lambda = \overline{x} - 0.5772\delta \tag{6}$$

where s and $\overline{x}$ are the standard deviation and the sample mean of the defects, respectively. Fig. 7 shows the distribution of defect sizes as described by the Gumbel extreme value distribution.

To define the return period used for defect size extrapolation, the following ratio was adopted:

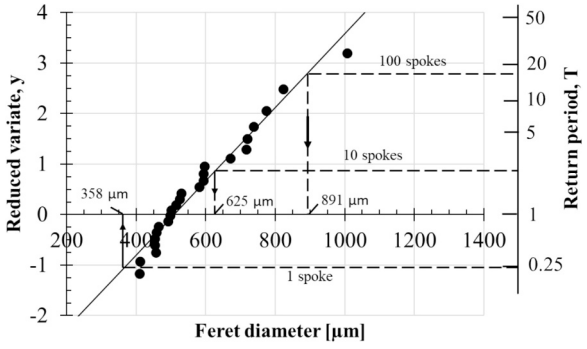

Fig. 7. Extreme value statistical distribution of maximum Feret dimensions ($A_0 = 120mm^2$).

$$T = \frac{A}{A_0} \tag{7}$$

with A_0 the metallographic inspection area and A is the area of interest for prediction. According to Murakami et al. [7], only the most stressed regions, where fatigue cracks are more likely to initiate, were considered for prediction. Specifically, the area corresponding to stress levels ranging between 100 and 90% of the maximum radial stress, as determined by FEA, was selected as A. To extend the analysis from the single critical structural detail to the industrial production scale, additional return periods were considered by referring to ten spokes, corresponding to one wheel, and one hundred spokes, corresponding to a batch of ten wheels. The corresponding maximum Feret diameters were then extrapolated from the fitted Gumbel distribution. In this way, the statistical analysis provides not only the expected maximum defect size for a single spoke, but also increasingly conservative defect estimates representative of larger production volumes. The resulting values are reported in Table 3 and were subsequently used to derive the lower-bound fatigue predictions discussed in Section 6.

After the return period was calculated, the corresponding largest maximum size of a defect with return period T is:

$$x(T) = \lambda + \delta \ln T \tag{8}$$

The resulting extrapolated maximum Feret diameters are reported in Table 3 for the three return periods considered, i.e. 1 spoke, 10 spokes, and 100 spokes. The values listed in Table 3 were subsequently used to derive the lower-bound fatigue predictions discussed in Section 6. In Fig. 7, auxiliary guide lines are also included to improve the readability of the extrapolation procedure and to show more clearly how the maximum Feret diameter associated with a given return period was obtained from the Gumbel plot.

5. Residual stress measurement

Residual stress measurements were carried out according to ASTM E837 Standard [33], using the SINT-Restan MTS3000 system, which features a high-precision micro-milling platform equipped with a high-speed air turbine (up to 300,000 rpm) and a stepper-motor-controlled feed mechanism. The system is operated through dedicated software that includes a data-processing module based on Schajer's integral method [34], allowing the reconstruction of non-uniform residual stress profiles along the depth of the drilled hole.

Three-element strain-gauge rosettes (HBM 1-RY61-1.5/120R) were bonded to the rear surface of three spokes, in the most critical region where fatigue cracks developed during the tests (see Fig. 8). Drilling was performed using tungsten-carbide end mills with a nominal diameter of 1.6 mm. A new cutter was used for each test to ensure consistency and accuracy. The feed rate was set to 0.2 mm/min and the final depth of 1 mm was reached through 20 increments of 0.05 mm. A dwell time of 5 s between consecutive steps was introduced to limit thermal effects.

Fig. 9 illustrates the distribution of the residual stress directed along the spoke axis (elaborated from the measured residual principal stresses) with respect to the depth. It should be reminded that, for confidentiality reasons related to industrial constraints, also the residual stress values reported in this figure are normalised with respect to the minimum level of the radial stress along the spoke axis applied during the bench tests.

Overall, the residual stress field detected on the rear side of the spokes is consistently compressive. Furthermore, the radial residual stresses were almost constant within 0.2 mm from the surface, where they present a normalised value roughly in the range 25 ÷ 45%. This compressive state effectively reduces the local mean stress during the rotating-bending tests, partially counteracting the tensile component produced by the external load. Since fatigue cracks were observed to nucleate at or very near the surface and to propagate along the surface region, the near-surface portion of the residual-stress profile is the most relevant for the predictive algorithm and was therefore considered sufficient for its definition. Although a detailed discussion of its impact on fatigue crack initiation is provided in the next section, it is worth noting here that both the magnitude and the distribution of the measured stresses are fully consistent with the component's manufacturing route and with the fatigue behaviour observed in the wheels. These findings indicate that the spokes retain a stabilizing compressive field capable of influencing crack-initiation conditions under service-like cyclic loading.

6. Fatigue limit and finite life prediction

This section describes the approach used to predict the fatigue limit and finite life of the A356-T6 wheels, considering inherent defects, i.e. the shrinkage pores detected by the micrographic analyses, as starting fatigue cracks. Specifically, the fatigue limit is determined by the well known Murakami's formula [7], while finite life is assessed by the approach recently proposed by Endo et al.

Table 3
Gumbel statistical parameters and extrapolated maximum Feret diameters for increasing return periods corresponding to 1 spoke, 10 spokes (1 wheel), and 100 spokes (10 wheels).

	Statistical parameters		Largest defect estimation	
	δ_{ML}	λ_{ML}	T	Feret [μm]
1 spoke	116.52	515.37	0.258	358
10 spokes			2.58	625
100 spokes			25.8	891

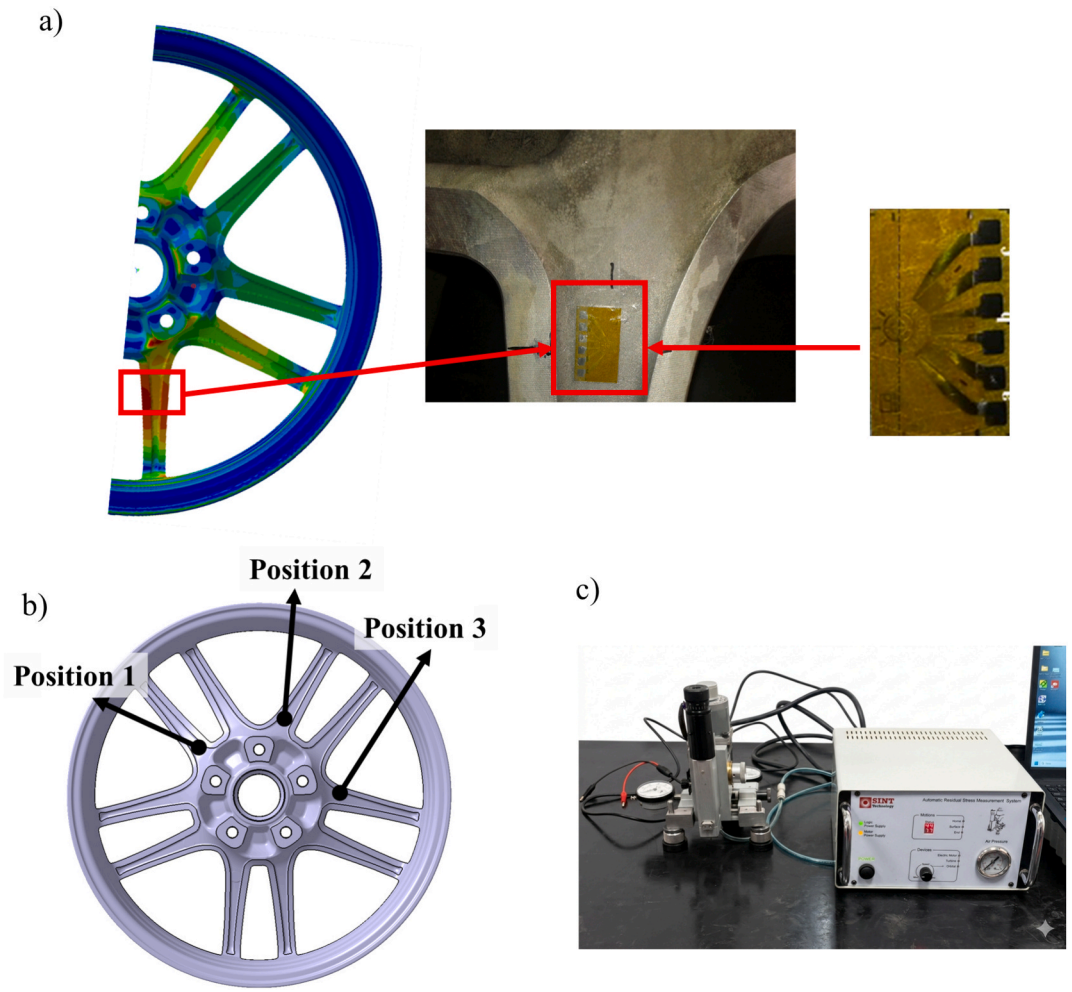

Fig. 8. Experimental setup used for residual stress measurements on the wheel spokes: a) Details of the measurement zone on the spoke; b) The three spokes selected for the measurements; c) The drilling apparatus.

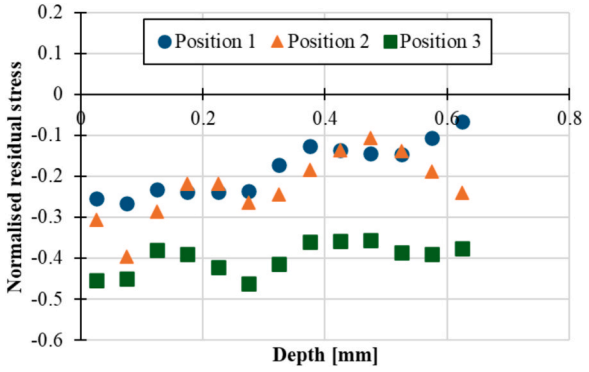

Fig. 9. Residual radial stress profiles measured by hole-drilling in the three wheel spokes.

[9] for the prediction of the S-N diagram, based on a small crack growth model (named as "scS-N prediction model") that accounts for the progressive reduction of the fatigue limit as the defect propagates [8,35]. In the case of stress ratio $R \neq -1$, an iterative procedure is required to determine the equivalent fatigue limit σ_w as a function of both the Vickers hardness HV and the mean stress [9]. For optimal comprehension of the method's application, a comprehensive flowchart detailing the entire sequence is provided in Fig. 10.

6.1. Predictive models

The fatigue limit under fully reversed loading $\sigma'_{w,R=-1}$ is first computed based on the original $\sqrt{area}$ parameter model, originally formulated and validated for standard steels. As discussed in [8,9,35], when this formulation is extended to other material classes, non-conservative predictions may arise and a practical correction is often introduced, for example by reducing the original threshold to 80% of its value. In the present work, the same rationale is adopted by introducing a correction factor F ($F < 1$), which is calibrated for the specific A356-T6 wheel condition investigated here. Assuming failures originate from surface or near-surface casting defects, the modified threshold is:

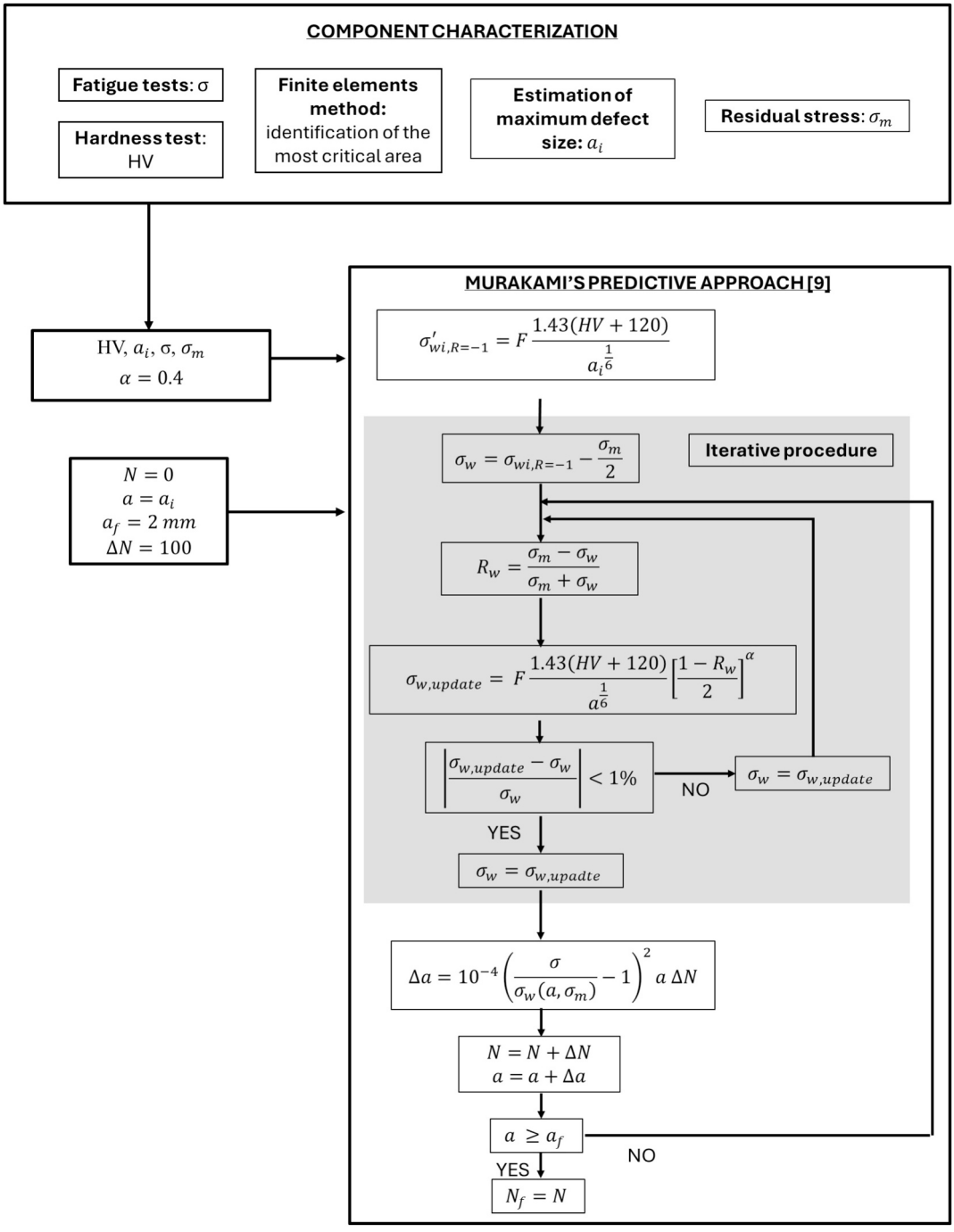

Fig. 10. Flowchart of the integrated defect-tolerant fatigue prediction methodology.

$$\sigma'_{w,R=-1} = F\frac{1.43(HV+120)}{a_i^{\frac{1}{6}}} \tag{9}$$

a_i is the initial defect size in terms of the expected maximum Feret diameter predicted by the statistical analysis. Once F is determined, it can be consistently applied to the same wheel products.

The fatigue limit σ_w under mean stress for the initial defect is:

$$\sigma_w = \sigma_{w,R=-1}\left[\frac{1-R_w}{2}\right]^{\alpha} \tag{10}$$

with $\alpha = 0.4$ and the auxiliary parameter R_w defined as:

$$R_w = \frac{\sigma_m - \sigma_w}{\sigma_m + \sigma_w} \tag{11}$$

The iterative procedure is initialized using the linear estimate:

$$\sigma_{wi} = \sigma_{wi,R=-1} - \frac{\sigma_m}{2} \tag{12}$$

This value evolves during crack propagation because σ_w depends on the instantaneous crack size. For a generic defect size a under mean stress σ_m, the updated threshold is obtained iteratively as:

$$\sigma_w(a,\sigma_m) = \sigma_{w,R=-1}\left[\frac{1-R_w}{2}\right]^{\alpha} = F\frac{1.43(HV+120)}{a_i^{\frac{1}{6}}}\left[\frac{1-R_w}{2}\right]^{\alpha} \tag{13}$$

Convergence is enforced by the following condition:

$$\left|\frac{\sigma_w^{(k+1)} - \sigma_w^{(k)}}{\sigma_w^{(k)}}\right| < 1\% \tag{14}$$

Crack propagation from the initial size a_i to the final critical size a_f is described by the small crack growth law:

$$\Delta a = C\left(\frac{\sigma}{\sigma_w(a,\sigma_m)} - 1\right)^m a^n \Delta N \tag{15}$$

To ensure strict dimensional consistency on both sides of the equation and recognizing that these terms act as nearly material-independent constants [8], the crack growth parameters are fixed to $C = 10^{-4}$, $m = 2$ and $n = 1$. Since σ_w depends on both a and σ_m, this equation is integrated numerically with cycle increments ΔN. At each increment, the fatigue limit is updated using the mean-stress correction, and the crack size is increased until $a = a_f$. The total predicted fatigue life is:

$$N_f = \sum N \tag{16}$$

such that

$$a(N_f) = a_f \tag{17}$$

6.2. Model calibration and validation

Before the calibration procedure, it is important to note that the model can also operate using normalised stress data. This is possible because all governing equations are expressed in terms of stress ratios rather than absolute stress values. As a result, the entire formulation remains valid even when stresses are scaled by a constant reference level.

Following the generalized approach for the scS-N model, the calibration was made using the experimental S-N dataset. For this purpose, experimental data from wheels that exhibited fractures originating from surface or near-surface casting defects were utilized, thereby validating the use of the geometric coefficient 1.43 in the threshold equation. Specifically, the calibration was anchored to a tested wheel where the exact size of the nucleating defect was measured via SEM. The operating conditions for this specimen involved a normalised stress amplitude of 1.05 and a local normalised mean stress of − 0.36 (induced by the compressive residual stress field). The initiating defect had an initial size of 226 μm, leading to component failure after about 950,000 cycles.

The calibration of the correction factor F was carried out using a non-linear optimization algorithm implemented in MATLAB. The objective function to be minimized is defined as the squared error between the base-10 logarithm of the experimental cycles to failure and the logarithm of the cycles predicted by the scS-N growth model. During the optimization loop, the algorithm numerically integrates the crack growth law, dynamically updating the local fatigue limit threshold at each increment to account for the instantaneous defect size and the mean stress effect. The result obtained from the calibration is $F = 0.73$.

The integrated S-N diagram, illustrated in Fig. 11, combines the experimental fatigue results with the predictive curves generated by the calibrated small-crack growth model. To account for the stochastic nature of casting defects in mass production, the framework

incorporates statistical lower bounds based on the Gumbel extreme value distribution. The dashed lines represent the predicted fatigue life as the defect size varies according to the inspected volume; specifically, curves were generated for one spoke, ten spokes (representing a single wheel), and one hundred spokes (representing a batch of ten wheels). As the return period increases, the statistically expected maximum Feret diameter grows, resulting in a downward shift of the S-N curves. The 1-spoke prediction was adopted as the practical fatigue threshold for the investigated wheel, since all experimental observations were located above this curve.

This difference between the individual experimental run-out and the predicted lower bounds highlights the core value of the proposed methodology. While the experimental run-out at a normalized stress level of 1.0 confirms the endurance of a single component, it does not account for the statistical probability of larger, more detrimental defects occurring in a wider production batch. By extending the analysis to return periods corresponding to ten and one hundred spokes, the model quantifies the influence of increasingly severe defect populations that may be encountered as the inspected volume increases. This approach shifts the focus from traditional testing, which only characterizes the specific specimens under load, to a proactive defect-tolerant design strategy. Consequently, the 1-spoke S-N curve serves as a robust industrial benchmark, providing a conservative threshold for the investigated wheel configuration, while the 10-spoke and 100-spoke predictions represent progressively more conservative scenarios associated with larger production volumes.

7. Conclusions

This study presented an integrated methodological approach for predicting the fatigue life of A356-T6 alloy wheels, based on the direct link between the microstructural defect population and the macroscopic performance of the component. The logical path of the research progressed from the systematic characterization of shrinkage porosity and its modelling through Gumbel extreme value statistics to the translation of this information into fatigue life predictions via the implementation of the Murakami-Endo small-crack growth model. By integrating physically consistent propagation parameters and a calibration procedure anchored to precise SEM experimental observations, the statistical variability of defects was transformed into reliability bands for industrial design, overcoming the limitations of traditional empirical models. Based on this methodological flow, the following conclusions can be drawn:

- Micrographic analysis combined with extreme-value statistics confirmed that fatigue endurance is governed by the extreme tail of the defect population. The maximum Feret diameter proved to be a reliable geometric parameter for describing the severity of the pores acting as nucleation sites.
- The adoption of the scS-N model allowed for a prediction based on physical criteria. By using material-independent propagation constants and normalizing stresses against a reference value, the framework ensures both dimensional consistency and generality of the results.
- The calibration of the model on a specific defect measured via SEM led to the determination of a material correction factor $F = 0.73$. This parameter enables the adaptation of Murakami's theoretical threshold to the specific response of the A356-T6 alloy without losing the rigor of the original equation.
- The predicted S-N curves for various return periods (1, 10, and 100 spokes) effectively serve as lower bounds for the experimental scatter. In particular, the 1-spoke curve represents a conservative and robust indicator, as all experimental data and run-outs were safely positioned above this limit.

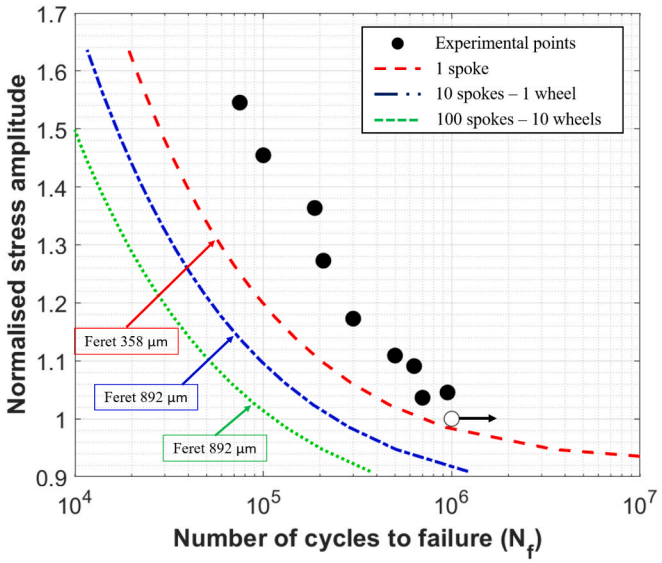

Fig. 11. Comparison between experimental fatigue results and scS-N model lower-bound predictions.

The integrated approach developed in this study provides a scientifically rigorous and industrially applicable methodology for fatigue life assessment. By connecting the gap between microstructural observations and statistical lower-bound predictions, this framework offers a powerful tool for the design of safer and more reliable automotive components.

CRediT authorship contribution statement

Nicola Zani: Writing – review & editing, Writing – original draft, Visualization, Validation, Methodology, Investigation, Data curation, Conceptualization. **Candida Petrogalli:** Writing – review & editing, Writing – original draft, Visualization, Validation, Methodology, Investigation, Data curation, Conceptualization. **Silvio Bonometti:** Methodology, Investigation, Data curation. **Nicola Ferrami:** Resources, Data curation. **Alessandro Concoreggi:** Resources, Data curation. **Alessio Franchi:** Resources, Data curation. **Claudio Sorlini:** Supervision, Resources, Data curation. **Giorgio Donzella:** Writing – review & editing, Validation, Supervision, Methodology, Investigation, Data curation, Conceptualization.

Declaration of competing interest

The authors declare that they have no known competing financial interests or personal relationships that could have appeared to influence the work reported in this paper.

Data availability

Absolute stress values are confidential due to industrial secrecy, other data are avalilable on request

References

[1] McDowell DL, Gall K, Horstemeyer MF, Fan J. Microstructure-based fatigue modeling of cast A356-T6 alloy. Engng Fract Mech 2003;70:49–80. https://doi.org/10.1016/S0013-7944(02)00021-8.
[2] Ammar HR, Samuel AM, Samuel FH. Effect of casting imperfections on the fatigue life of 319-F and A356-T6 Al-Si casting alloys. Mater Sci Engng A 2008;473:65–75. https://doi.org/10.1016/j.msea.2007.03.112.
[3] Zhang Y, Xu J, Zhai T. Distributions of pore size and fatigue weak link strength in an A713 sand cast aluminum alloy. Mater Sci Engng A 2010;527:3639–44. https://doi.org/10.1016/j.msea.2010.03.104.
[4] Y.X. Gao, T. C. Lindley, J.Z. Yi, P.D. Lee, Fatigue Fract Eng Mat Struct - 2004 - GAO - The effect of porosity on the fatigue life of cast aluminium-silicon alloys.pdf, (n.d.).
[5] Uematsu Y, Kakiuchi T, Tajiri A, Nakajima M. Fatigue limit prediction of A356-T6 cast aluminum alloys with different defect sizes sampled from an actual large-scale component. Int J Struct Integr 2017;8:617–31. https://doi.org/10.1108/IJSI-12-2016-0038.
[6] Dey A, Jugade H, Jain V, Adhikary M. Cracking phenomena in automotive wheels: an insight. Engng Fail Anal 2019;105:1273–86. https://doi.org/10.1016/j.engfailanal.2019.01.069.
[7] Murakami Y. Metal fatigue: effects of small defects and nonmetallic inclusions. Oxford: Elsevier; 2002.
[8] Murakami Y, Endo M. Prediction model of S-N curve without fatigue test or with a minimum number of fatigue tests. Engng Fail Anal 2023;154:107647. https://doi.org/10.1016/j.engfailanal.2023.107647.
[9] Endo M, Murakami Y. Prediction model of S-N curve under mean stress without fatigue test or with a minimum number of fatigue tests. Theor Appl Fract Mech 2025;138:104918. https://doi.org/10.1016/j.tafmec.2025.104918.
[10] Buffière JY, Savelli S, Jouneau PH, Maire E, Fougères R. Experimental study of porosity and its relation to fatigue mechanisms of model Al-Si7-MgO.3 cast Al alloys. Mater Sci Eng A 316 2001:115–26. https://doi.org/10.1016/S0921-5093(01)01225-4.
[11] Konečná R, Fintová S, Nicoletto G. Shrinkage pores and fatigue behavior of cast Al-Si alloys. Key Engng Mater 2011;465:354–7. https://doi.org/10.4028/www.scientific.net/KEM.465.354.
[12] Konečná R, Nicoletto G, Fintová S. Statistical description of largest pore sizes in cast Al-Si alloys, Proc. - 25th Danubia-Adria Symp. Adv Exp Mech DAS 2019;2008(16):123–4.
[13] Li S, Han J, Wang J, Liu D, Guo S, Bi J, et al. Defects and fatigue properties of LPDC-fabricated aluminum alloy wheel: Experimental and numerical simulation methods. Engng Fail Anal 2025;182:110074. https://doi.org/10.1016/j.engfailanal.2025.110074.
[14] Tebaldini M, Petrogalli C, Donzella G, Gelfi M, La Vecchia GM. A356-T6 wheels: influence of casting defects on fatigue design. Fatigue Fract Eng Mat Struct 2018;41:1784–93.
[15] Brueckner-Foit A, Luetje M, Bacaicoa I, Geisert A, Fehlbier M. On the role of internal defects in the fatigue damage process of a cast Al-Si-Cu alloy. Procedia Struct Integr 2017;7:36–43. https://doi.org/10.1016/j.prostr.2017.11.058.
[16] Beretta S. More than 25 years of extreme value statistics for defects: fundamentals, historical developments, recent applications. Int J Fatigue 2021;151:106407. https://doi.org/10.1016/j.ijfatigue.2021.106407.
[17] Matsuda S, Hashimoto T, Takamatsu K, Matsuo T, Endo M, Yamabe J. Crack initiation and propagation behaviors in rotating bending fatigue of Al-Si-Mg cast aluminum alloy containing artificial defects and applicability of the $\sqrt{\text{area}}$ parameter model. Procedia Struct Integr 2025;71:4–9. https://doi.org/10.1016/j.prostr.2025.08.002.
[18] Wang S, Li Z, Ma X, Wu X, Kong D, Qiao H, et al. Integrated predictions of the influence of mesh size, casting defects and SDAS on the fatigue life of aluminum alloy wheels. J Mater Res Technol 2025;35:3956–67. https://doi.org/10.1016/j.jmrt.2025.02.091.
[19] Wang S, Li Z, Qiao H, Hou Q, Kong D, Wu X, et al. Multi-scale fatigue life prediction method of the A356 wheel considering the effects of casting microstructure. Int J Fatigue 2025;198:108977. https://doi.org/10.1016/j.ijfatigue.2025.108977.
[20] Allouch S, Bleicher C, Krause I, Tank J. Fatigue life of wheels regarding design and test constraints. Procedia Struct Integr 2025;75:299–310. https://doi.org/10.1016/j.prostr.2025.11.031.
[21] Zanchini M, Longhi D, Mantovani S, Puglisi F, Giacalone M. Fatigue and failure analysis of aluminium and composite automotive wheel rims: Experimental and numerical investigation. Engng Fail Anal 2023;146:107064. https://doi.org/10.1016/j.engfailanal.2023.107064.
[22] Yang H, Cui Y, Qin F, Lin T, Zheng Y. Fatigue failure analysis and life prediction of forged 6061 aluminum alloy wheel hubs based on precipitate size effects and multiaxial stress modeling. Engng Fail Anal 2025;182:110181. https://doi.org/10.1016/j.engfailanal.2025.110181.
[23] Carboni M, Beretta S, Finzi A. Defects and in-service fatigue life of truck wheels. Engng Fail Anal 2003;10:45–57. https://doi.org/10.1016/S1350-6307(02)00036-5.
[24] Zerbst U, Madia M, Klinger C, Bettge D, Murakami Y. Defects as a root cause of fatigue failure of metallic components. II: Non-metallic inclusions. Engng Fail Anal 2019;98:228–39. https://doi.org/10.1016/J.ENGFAILANAL.2019.01.054.

[25] Zerbst U, Madia M, Klinger C, Bettge D, Murakami Y. Defects as a root cause of fatigue failure of metallic components. I: basic aspects. Engng Fail Anal 2019;97:777–92. https://doi.org/10.1016/J.ENGFAILANAL.2019.01.055.
[26] Casellas D, Pérez R, Prado JM. Fatigue variability in Al-Si cast alloys. Mater Sci Engng A 2005;398:171–9. https://doi.org/10.1016/j.msea.2005.03.034.
[27] Serrano-Munoz I, Buffiere JY, Verdu C, Gaillard Y, Mu P, Nadot Y. Influence of surface and internal casting defects on the fatigue behaviour of A357-T6 cast aluminium alloy. Int J Fatigue 2016;82:361–70. https://doi.org/10.1016/J.IJFATIGUE.2015.07.032.
[28] SAE J328:2021 Wheels - Passenger Car and Light Truck Performance Requirements and Test Procedures, SAE Technical Papers. (2021). https://doi.org/10.4271/J328_202107.
[29] ASTM E3-11, Standard Guide for Preparation of Metallographic Specimens, ASTM International, 2011.
[30] ASTM E2283-03, Standard Practice for Extreme Value Analysis of Nonmetallic Inclusions in Steel and Other Microstructural Features, ASTM International, 2003.
[31] ESIS P11-02, Procedure for Extreme Value Defect Analysis of Inclusion/Defect Size, European Structural Integrity Society (ESIS), 2002.
[32] Gumbel EJ. Statistics of Extremes. Mineola, NY: Dover Publications; 2004.
[33] ASTM E837-20, Standard Test Method for Determining Residual Stresses using the Hole-Drilling Strain-Gage Method, ASTM International, (n.d.) 837.
[34] Schajer G. Measurement of non-uniform residual stresses using the hole drilling method. J Engng Mater Technol 1998;43:1–9.
[35] Murakami Y, Takagi T, Wada K, Matsunaga H. Essential structure of S-N curve: prediction of fatigue life and fatigue limit of defective materials and nature of scatter. Int J Fatigue 2021;146:106138. https://doi.org/10.1016/J.IJFATIGUE.2020.106138.